

Microwave-free wide-field magnetometry using nitrogen-vacancy centers

Joseph Shaji Rebeirro^{1,2,*}, Muhib Omar,^{1,2} Till Lenz,^{1,2} Omkar Dhungel,^{1,2} Peter Blümller¹, Dmitry Budker,^{1,2,3} and Arne Wickenbrock^{1,2,†}

¹*Johannes Gutenberg-Universität Mainz, Mainz 55128, Germany*

²*Helmholtz-Institut Mainz, GSI Helmholtzzentrum für Schwerionenforschung, Mainz 55128, Germany*

³*Department of Physics, University of California, Berkeley, California 94720, USA*

(Received 30 October 2023; revised 18 March 2024; accepted 20 March 2024; published 22 April 2024)

A wide-field magnetometer utilizing nitrogen-vacancy ($N-V$) centers in diamond that does not require microwaves is demonstrated. It is designed for applications where microwaves need to be avoided, such as magnetic imaging of biological or conductive samples. The system exploits a magnetically sensitive feature of $N-V$ centers near the ground-state level anticrossing (GSLAC). An applied test field from a wire has been mapped over an imaging area of $\approx 500 \times 470 \mu\text{m}^2$. Analysis of the ground-state level anticrossing (GSLAC) lineshape allows us to extract the vector information of the applied field. The device allows micrometer-scale magnetic imaging at a spatial resolution dominated by the thickness of the $N-V$ layer (here, $50 \mu\text{m}$). For a pixel size of $4 \mu\text{m} \times 3.8 \mu\text{m}$, the estimated photon-shot-noise-limited sensitivity is $4.8 \mu\text{T}/\sqrt{\text{Hz}}$. Two modalities for visualizing the magnetic fields, static and temporal, are presented, along with a discussion of technical limitations and future extensions of the method.

DOI: [10.1103/PhysRevApplied.21.044039](https://doi.org/10.1103/PhysRevApplied.21.044039)

I. INTRODUCTION

Negatively charged ($N-V$) centers in diamond [1] have attracted significant attention as a promising platform for sensing various physical quantities, such as temperature, pressure, and magnetic and electric fields, at the nanoscale under various environmental conditions [2–4]. Magnetometry based on spin-dependent fluorescence of these $N-V$ centers has demonstrated sensitivities down to $0.6 \text{ pT}/\sqrt{\text{Hz}}$ for ensembles at room temperature [5–7]. By employing optically detected magnetic resonance (ODMR) with $N-V$ centers, one can probe the magnetic fields generated by a wide range of samples, including biological systems, magnetic materials, current-carrying wires, and field-programmable gate arrays (FPGAs) [6,8–11]. In optically detected magnetic resonance (ODMR) based magnetometry, a diamond sample is illuminated with laser light (e.g., at 532 nm) and is subjected to a microwave field to drive population transfer between the differently bright spin states. When the microwave frequency matches a transition, there is a decrease in fluorescence. Measuring the resonant frequencies for transitions between the $m_s = 0$ and $m_s = \pm 1$ states allows reconstruction of the magnetic field projection onto the $N-V$ axis [4,12,13].

However, there are scenarios in which the use of microwaves is undesirable, such as when dealing with conductive materials or sensitive biological samples. To address this, recent developments have focused on microwave-free protocols that exploit energy-level crossings of $N-V$ centers at different magnetic fields. These protocols include microwave-free magnetometry and vector magnetometry at zero field, as well as the exploitation of specific features such as the excited-state level anticrossing (ESLAC) feature at 51.2 mT and the ground-state level anticrossing (GSLAC) feature at 102.45 mT [13–15]. These kinds of magnetically sensitive features have been successfully utilized for vector magnetometry, measuring eddy currents in conducting materials and performing nuclear magnetic resonance (NMR) [16–18]. In light of these advancements, here, we present a microwave-free wide-field magnetic microscope that leverages the ground-state level anticrossing (GSLAC) feature to probe and image samples where microwaves are detrimental.

The GSLAC feature originates from the mixing of ground-state levels at 102.45 mT . Due to the Zeeman splitting of the triplet ground state, as illustrated in Fig. 1(a), the $m_s = -1$ state becomes degenerate with the $m_s = 0$ state and mixing results in population transfer between these states. Mixing occurs due to hyperfine interaction and cross relaxation with other defects as well as static and oscillating transversal magnetic fields. The population transfer is observed as a drop in the fluorescence intensity.

*Corresponding authors: jshajire@students.uni-mainz.de

†wickenbr@uni-mainz.de

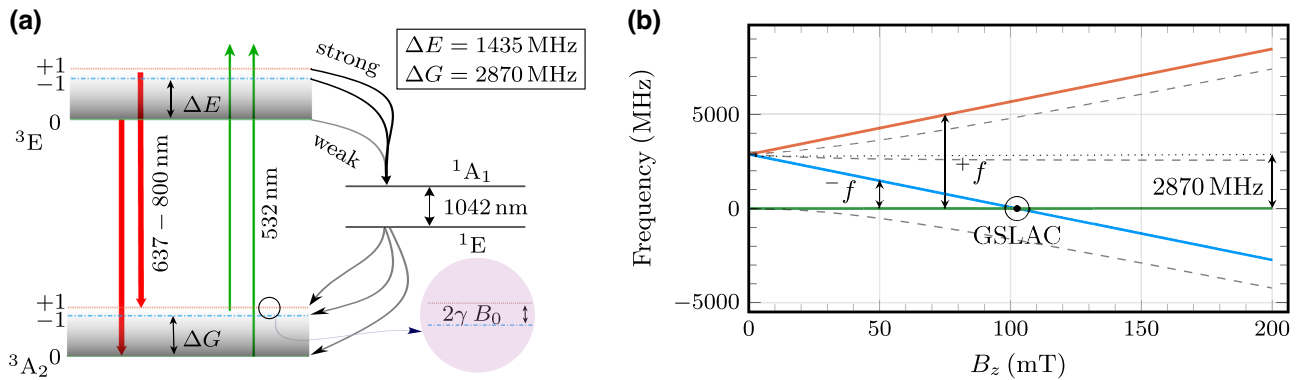


FIG. 1. (a) The energy levels of a $N-V^-$ center [12], also showing the intersystem crossing (ISC) from $^3E \rightarrow ^1A_1 \rightarrow ^1E \rightarrow ^3A_2$, respectively. Two transition pathways, with and without the ISC, are indicated. The green and red arrows represent excitation and decay from and to the electronic ground-state triplet; the black curves (“strong” and “weak”) represent decay via the ISC. Strong and weak in this context means higher and lower rates of decay. The gray gradient is used to indicate the phonon sidebands of the respective triplets. (b) The energy levels of the $N-V$ center as a function of B_z of the electron-spin magnetic sublevels of the ground-state triplet, neglecting hyperfine structure. The colored solid lines represent the $N-V$ -center axes aligned with the magnetic field of the Halbach assembly. These on-axis $N-V$ -center axes contribute to the GSLAC feature. The dashed black lines represent the other $N-V$ -center axes, positioned 109.37° from the magnetic field of the Halbach assembly due to tetrahedral symmetry. As such, the energy levels of the $N-V$ centers off axis to the magnetic field do not cross at 102.45 mT , implying that there is no contribution to the GSLAC feature [16,19].

Our study aims to explore the potential of utilizing $N-V$ centers without the need for microwaves to map magnetic fields. We create static magnetic field maps by analyzing the lineshape of the GSLAC resonance pixel by pixel. Furthermore, in another sensing modality, we investigate the sensitivity to dynamic field changes between individual image frames.

To demonstrate the utility of this magnetometer, we map the magnetic field distribution of a direct-current (dc) field generated by a straight current-carrying wire with a diameter of $200 \mu\text{m}$ placed on the diamond sample while we image it from underneath. This proof-of-concept experiment explores the application of $N-V$ centers in a setup without microwaves. The lack of microwaves increases the usability of the device while reducing its technical complexity, since no microwave components are needed. The results highlight the viability of diamond-based quantum sensors for a wide range of materials and biological applications.

II. EXPERIMENTAL SETUP

The setup incorporates a Halbach assembly [20,21], two pairs of coils, a (110) diamond plate, and collection optics. The cylindrical Halbach assembly provides a magnetic field orthogonal to its bore with minimal stray field external to the magnet. The diamond is chemical vapor deposition (CVD) grown and obtained from Element Six, with a concentration of 3.7 ppm homogeneously distributed $N-V$ centers. It has been cut mechanically from a ^{13}C -depleted Ib diamond with a (100) face to a

(110) face. The dimensions of the diamond sample are $1 \times 0.5 \times 0.05 \text{ mm}^3$. It has an initial nitrogen concentration $\leq 10 \text{ ppm}$. It has been irradiated with electrons of 5 MeV, with a electron dose of $2 \times 10^{19} \text{ cm}^{-2}$ and then annealed at 700°C for 8 h. The thickness of the $N-V$ layer ($50 \mu\text{m}$) limits the spatial magnetic field resolution [22]. The diamond is shown in Fig. 2(b), where the field of view is marked in blue and the two $N-V$ axes of the diamond orthogonal to the cylinder bore that are usable for microwave-free magnetometry are marked in yellow and violet. We use the orientation marked in violet.

The sample is positioned in the center of the Halbach assembly on a rotatable platform, with its axis of rotation parallel to the Halbach assembly bore perpendicular to the field. This allows us to align the $N-V$ axis in the (110) plane of the diamond to the Halbach assembly background field produced. The sample is set on a sapphire window with a diameter of 10 mm and a thickness of 0.25 mm. It permits laser-light delivery and collection of light from under the diamond sample while acting as a heat sink. As shown in Fig. 2, the Halbach assembly is fitted with two sets of Helmholtz-coil pairs. Coil pair C_1 is oriented in the direction of the background field and coil pair C_2 is perpendicular to it and parallel to the cylinder axis. The coils are used to shim the magnetic field of the Halbach assembly and optimize the linewidth and contrast of the GSLAC feature. The diamond mount is attached to the C_1 coils. It features a range of $\pm 1.3 \text{ mT}$. The second Helmholtz-coil pair (C_2) is used to remove residual transverse fields. A third coil pair perpendicular to C_1 and C_2 would be ideal

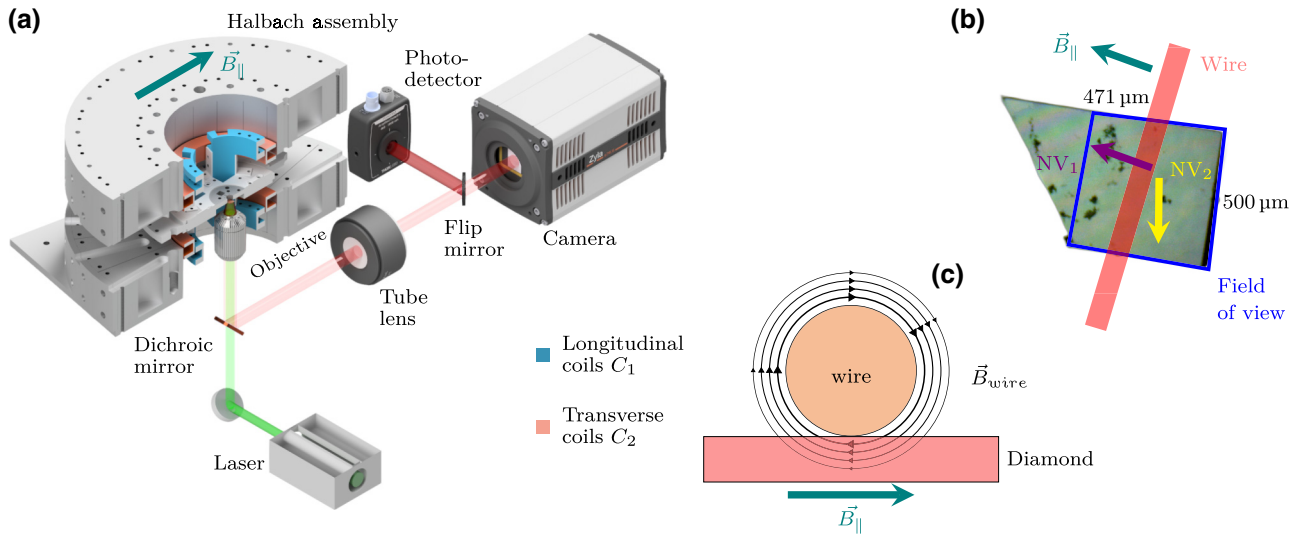


FIG. 2. (a) The wide-field imaging setup. It includes the diamond, an objective, and the light path. Longitudinal coils C_1 and transverse coils C_2 are used to offset the corresponding magnetic fields. The dichroic mirror is used to separate the collected fluorescence from the reflected green light and a flip mirror directs it either to a camera or a photodetector. The axis of the background magnetic field is denoted as \vec{B}_{\parallel} . (b) The [110] sample has been made from a [100] cut diamond. The dark areas are presumably dirt within the crystal that is resistant to acid cleaning. The unreliable data from these positions have been replaced with the mean of the five nearest reliable pixels. The thickness of the diamond is 50 μm , which sets the upper limit for spatial field resolution referred to in Ref. [22]. (c) An illustration of the magnetic field arrangement. The magnetic field by the wire \vec{B}_{wire} counteracts \vec{B}_{\parallel} from the Halbach assembly for positive currents.

but has not been implemented due to space constraints in the magnet bore.

A continuous-wave (cw) 532-nm laser (Laser Quantum, gem532) is used to illuminate the diamond via a microscope objective (Olympus Plan 10X objective). The fluorescent light is gathered using the same objective, reflected off a short-pass dichroic mirror with a cutoff wavelength of 600 nm, and passed through a long-pass filter to remove the remaining green reflection of the laser light.

The collected fluorescence is directed to a scientific complementary metal-oxide semiconductor (sCMOS) camera (Andor Zyla 5.5) for imaging. Alternatively, for diagnostic purposes, the light can be directed to a photodiode (PDA36A2) using a flip mirror.

III. RESULTS AND DISCUSSION

A. Static imaging

We have demonstrated a static magnetic field imaging modality using the GSLAC by visualizing the field generated by a wire carrying electric current. The results are presented in Fig. 3(b). To image, we have illuminated the diamond with cw 532-nm laser light with a Gaussian profile. The laser beam covers an area of $\approx 0.5 \times 0.47 \text{ mm}^2$.

The background magnetic field has been swept over a range of 102.45(130) mT, covering the GSLAC feature while images have been taken with the camera. In this way, the individual pixels contain a magnetic field scan

over the GSLAC feature. The current-carrying wire generates both axial (B_{\parallel}) and transverse components (B_{\perp}) in the measurement region, thereby leading to alterations in the contrast (C), the full width at half maximum (FWHM), and the center-field position of the GSLAC feature.

To analyze and quantify the observed changes, we have fitted the experimental data pixel by pixel with a Lorentzian function [23,24] to extract three fitting parameters: the contrast (C), the FWHM (Γ), and the center field (b).

To ensure synchronization between the magnetic field ramp and the data acquisition, we have employed an external trigger at 185 Hz. This trigger serves as a timing reference and triggers the camera to capture 70 frames during a 0.4-s magnetic field ramp.

Additionally, to enhance the signal-to-noise ratio, we have repeated the acquisition 20 times and averaged the results. The acquisition procedure, which is similar to that of [25], is illustrated in Fig. 3(a).

During data analysis, we have extracted the GSLAC feature from individual pixels within a specific region measuring . This region comprises a total of 625×715 pixels, with each pixel corresponding to an area of approximately $0.8 \mu\text{m} \times 0.69 \mu\text{m}$ on the diamond surface. The extracted data are averaged over a 5×5 pixels grid. This binning process reduces the optical resolution to approximately $4 \mu\text{m} \times 3.4 \mu\text{m}$, which does not limit the spatial resolution for magnetic fields.

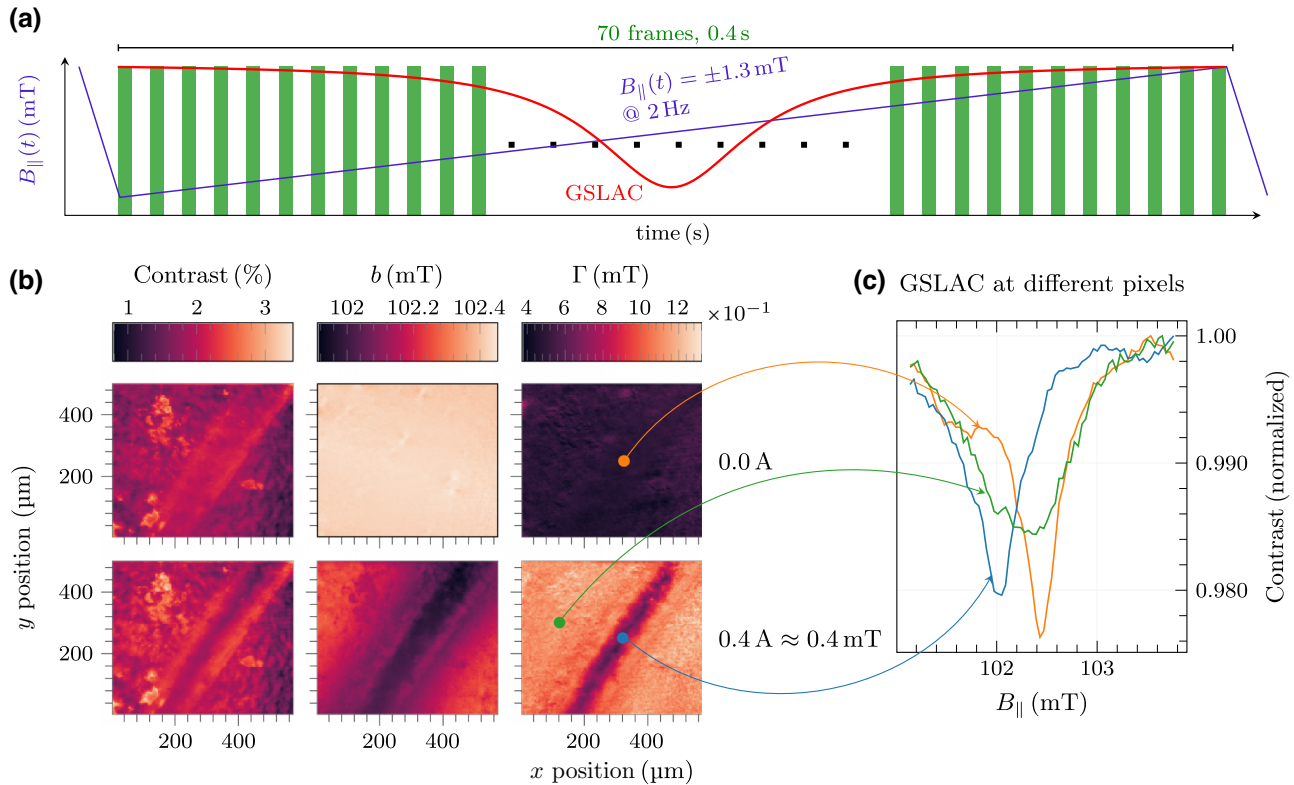


FIG. 3. (a) The experimental sequence: data collection using a camera to capture pictures at the rising edges of 70 external triggers operating at 185 Hz are synchronized with a magnetic field sweep. The blue ramp indicated in (a) represents the field sweep, while the red trace illustrates the GSLAC feature. (b) Magnetic field maps obtained from a dc field generated with a wire carrying 0 A and 0.4 A (top and bottom, respectively). Each image is the result of the analysis of magnetic field scans in each pixel where the signal profiles are fitted with a Lorentzian function. The contrast C , center field (b), and full width at half maximum (FWHM) (Γ) are then extracted and displayed. (c) The GSLAC examined at two positions in the diamond and a comparison of the results with the case without an applied test signal. The blue and orange traces are taken from the same position beneath the wire with and without a test signal. The green trace is for a position taken 200 μm away from the wire center. This indicates that the axial component of the test field is more prominent closer to the wire and that the transverse component is more prominent further away from the wire due to the curvature of the field, consistent with the illustration in Fig. 2(c). This is also apparent in Fig. 4.

We have utilized the Levenberg-Marquardt (LM) algorithm [26] to fit the binned data on a pixel-by-pixel basis to a Lorentzian function. We have extracted the fitting parameters for each pixel, which provides information about the magnetic field distribution. The fitting of multiple pixels has been done in parallel utilizing a threaded PYTHON script. The resulting data-processing time was 136 s per image. This is still significantly longer than the data-acquisition time and requires further improvement; e.g., by deploying a parallel fitting routine on a graphics card or a FPGA.

The maps presented in Fig. 3(b) are reconstructed images of a current-carrying wire. As the wire field in the sensor is mostly antialigned to the background field [see Fig. 2(c)], the total magnetic field decreases. The wire field results in a shift and a broadening of the GSLAC feature. On examination of the maps, we observe that the width of the feature is smallest at the center of the wire and increases away from it. This is mirrored in the center maps

[Figs. 2(c) and 3(c)], where the change in the total magnetic field is largest under the wire. This is consistent with a model of the wire magnetic field in the diamond.

No broadening of the GSLAC linewidth is visible under the wire due to the absence of transverse fields. Moving away from the center of the wire, the transverse magnetic field components increase, leading to a broadening of the FWHM of the GSLAC feature. The GSLAC center field maps (parameter b) in Fig. 3(b) show that the longitudinal component of the magnetic field decreases moving away from the wire. Close to the wire, the GSLAC feature shifts by 0.5 mT from 102.4 mT to 101.9 mT when a magnetic field corresponding to a current of 0.4 A is applied. This shift gradually reduces to 0.1 mT furthest from the wire in the image.

In principle, the measurements performed here contain vector information. The longitudinal part is linearly sensitive to the magnetic field in this direction and the linewidth is a function of the applied transverse field. Complete

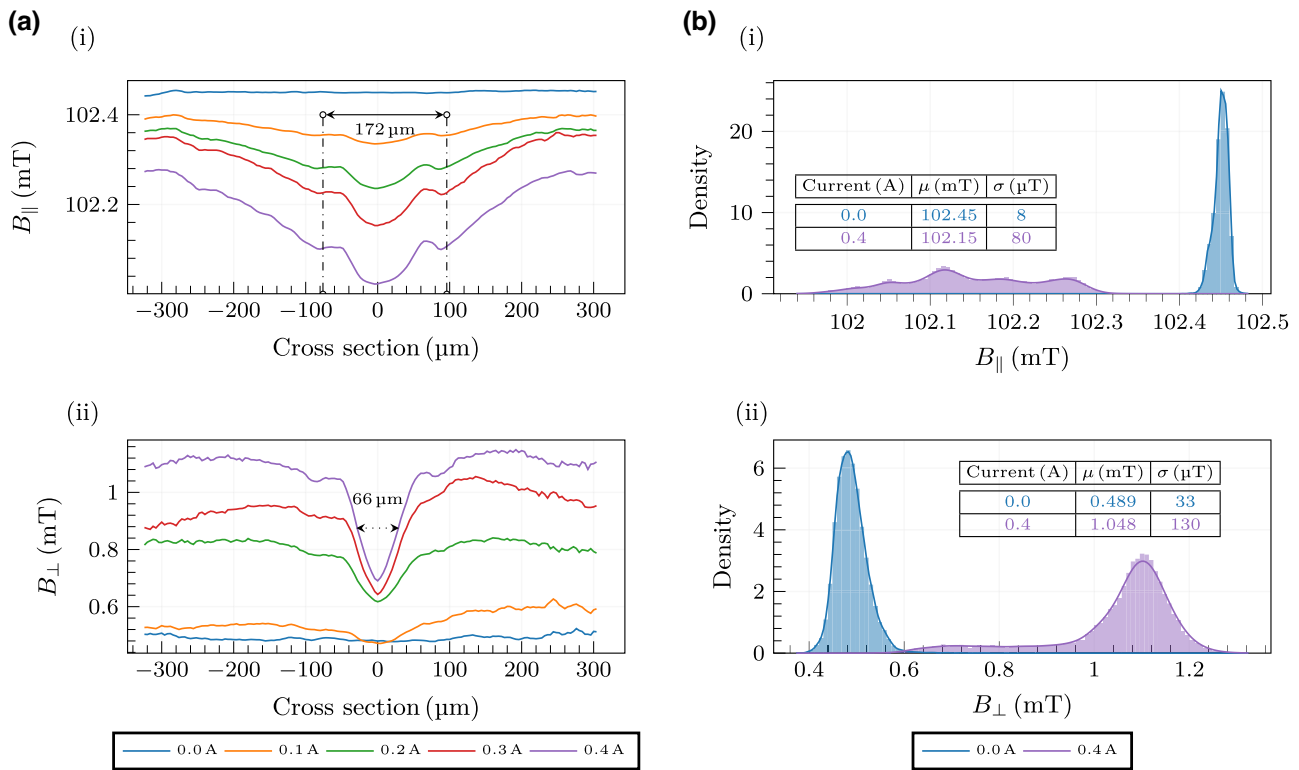


FIG. 4. (a) Cross sections of the center field (b) and the FWHM maps in Fig. 3(b) displayed for multiple currents, respectively. The cross section is perpendicular to the wire. The center shift is maximal under the wire (i), while the width has a minimum there (ii). This aligns with the expected pattern of the generated field, as the width is influenced by the transverse component of the field illustrated in Fig. 2(c). (b) (i) The distribution of the center field (b) (i) at the reference field (0 A) and the distribution when a test field (0.4 A) is applied with the mean and standard deviation annotated for each case. The reference-field distribution has a mean (μ) of 102.45 mT and a standard deviation (σ) of 8 μT , validating the homogeneity of the magnet as previously demonstrated [20,21]. (ii) Likewise, the FWHM (Γ) distribution for both cases. Both distributions have been obtained over the entire field of view.

vector reconstruction of the magnetic field is possible at the GSLAC and has been suggested and demonstrated in Ref. [16]. Expanding this technique to encompass full vector field imaging constitutes a topic for future research.

Additionally, we have examined an averaged cross section of the maps in Fig. 4, specifically focusing on the FWHM displayed in Fig. 4(b). We have observed something peculiar: considering the thickness of the N-V layer in the diamond, which is approximately 50 μm , the spatial resolution for the magnetic field was also expected to be on the order of 50 μm [22]. The wire itself has a diameter of 200 μm . From observation, however, the feature in Fig. 4(b) corresponding to the wire shows a FWHM of \approx 66 μm when a field is generated with a wire carrying 0.4 A. Just directly below the wire, its field does not feature a transverse component in the N-V layer. So just there, no broadening is observed. This effect becomes more pronounced with increasing wire current. This bears some resemblance to superresolution imaging techniques such as stimulated emission depletion (STED) [27,28], albeit in the context of magnetic fields. In STED, a laser beam with a donut-shaped cross section is used to deexcite emitters

through stimulated emission for subdiffraction resolution images.

B. Temporal imaging

To implement dynamic imaging, we have captured a video while pulsing current through the wire. This allows us to observe the magnetic field from the wire in real time. The results are summarized in Fig. 5. The temporal resolution is limited by the camera frame rate, which is set at 39 Hz. The camera can operate at a significantly higher frame rate; however, this reduces the amount of collected photons.

The experimental procedure is illustrated in Fig. 5(a). It involves tuning the bias field to the slope of the GSLAC feature in at 101.7 mT. We then capture 15 frames for 380 ms (at a rate of 39 Hz) while turning on a current of 0.4 A through the wire for the central 100 ms. Postacquisition, we normalize the contrast of each pixel by its maximum value in the 15 images. This allows a straightforward comparison of frames taken before and during the current pulse.

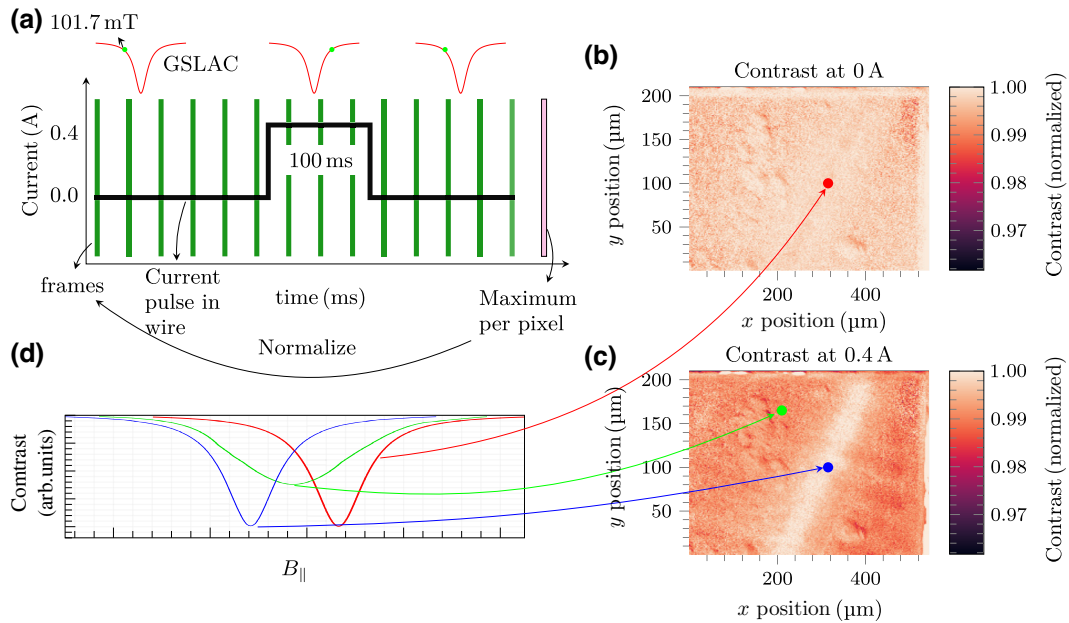


FIG. 5. (a) An illustration of the data-acquisition and processing sequence for temporal imaging. Fifteen frames have been taken at 39 Hz, while a current pulse has been applied during acquisition. The frames have been normalized to the maximum value per pixel to visualize dynamics. (b),(c) The dynamics between two frames with a temporal separation of 25 ms: (b) the contrast with no test signal; (c) the contrast variation induced when a current of 0.4 A generates a field. The field below the wire has been shifted to 103.2 mT, which causes it to appear brighter. The spatial resolution is restricted to $\approx 50 \mu\text{m}$, which is the resolution limit for magnetic features that can be attained with the WF sample. In the areas away from the wire, the GSLAC feature is broadened and shifted, which is observed as a reduction in contrast. (d) An illustration of the expected signal as a function of a magnetic field at three different positions in the acquired frames, for clarification of the processes involved.

In Figs. 5(b) and 5(c), we present two frames separated by 25 ms. In Fig. 5(b), no current is applied through the wire. In Fig. 5(c), a current of 0.4 A is applied. We observe changes in contrast in areas away from the wire. This is a result of the transverse components of the magnetic field (B_{\perp}) generated by the wire. It broadens the GSLAC feature. The broadening leads to a decrease in contrast and makes the corresponding diamond region appear darker. However, directly under the wire, the magnetic field is aligned with the total field ($B_{||}$), causing the GSLAC resonance to shift to 103.2 mT but not to broaden. This is why this region remains bright. We have chosen the values

of the bias and the wire fields to maximize the contrast variation between the “on” and “off” frames integrated over the complete image. Furthermore, we have chosen these parameters to ensure that all pixels remain within the GSLAC feature and to determine the limit of the contrast variations that we can visualize.

An analysis of the temporal cross section of the acquired frames is shown in Fig. 6(a). The applied pulse shape is retrieved. An examination of the cross section of the wire image is presented in Fig. 6(b). We discern maximum contrast variations of up to 9% at a distance of 100 μm from the wire center. Beyond this distance, the

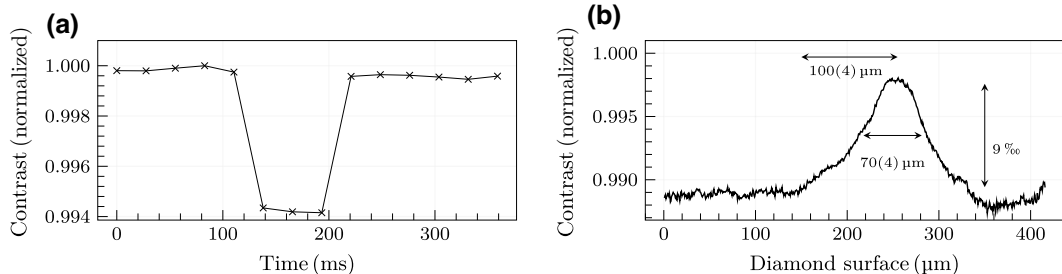


FIG. 6. (a) The mean values of the averaged contrast per frame throughout the acquisition, showing the applied pulse. (b) The mean values of the contrast for points in the direction orthogonal to the wire. We can detect a contrast drop of from 9% up to 100 μm from the center of the wire, after which the contrast variation saturates.

contrast variations, which are due mostly to the transverse field component of the wire, level off. To further improve the temporal and spatial resolution in this modality, high-frame-rate or lock-in detection-enabled cameras can be employed.

IV. CONCLUSIONS

We have developed a microwave-free diamond magnetic field microscope utilizing N-V centers to measure spatially varying magnetic fields over a field of view of approximately $500 \times 470 \mu\text{m}$. We have analyzed the GSLAC feature and can reconstruct longitudinal and transverse components of magnetic fields of samples. We have implemented a fitting algorithm to extract the GSLAC feature and estimate the magnetic fields in an image of 125×143 pixels postbinning.

Our results demonstrate the potential of microwave-free vector magnetometry with temporal resolution enabling the recording of magnetic “movies.” We envision that this approach will have a significant impact across a range of fields, including materials science, biology, and condensed-matter physics. It is important to acknowledge the limitations in achieving high-resolution magnetic maps using the current methodology. One constraint is that only 1/4 of the N-V-center orientations are available for this modality, due to the requirement of on-axis alignment with the bias field. This leads to an overall drop in signal [14,19]. The use of preferentially oriented N-V centers could enhance the overall contrast and sensitivity [30].

Another limitation arises from the camera, which imposes constraints in terms of its full well capacity (FWC) and frames per second [29]. The mean per-pixel shot-noise limit is estimated to be approximately

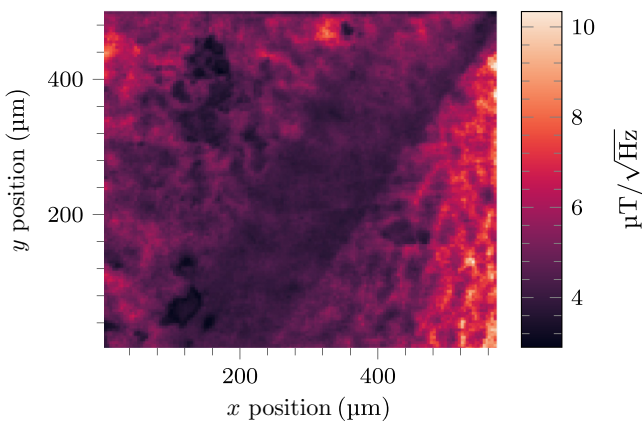


FIG. 7. The photon-shot-noise map, estimated using the FWHM and contrast maps shown in Fig. 3(b), employing the adapted equation for cameras as outlined in Ref. [29]. The volume-normalized estimate has been obtained by dividing the photon rate per pixel by the volume of diamond per pixel. This corresponds to a scaling factor of $28 \mu\text{m}$.

$4.8 \mu\text{T}/\sqrt{\text{Hz}}$ for a pixel size of $4 \mu\text{m}$ or $137.35 \mu\text{T} \mu\text{m}^{3/2}/\sqrt{\text{Hz}}$ for a volume-normalized estimate. The map of which is shown in Fig. 7. The scaling between volume-normalized and per-pixel sensitivity is approximately $28 \mu\text{m}$, which is the square root of the volume under the diamond.

This can be compared to the best-reported volume-normalized sensitivities of comparable cameras using microwaves (including lock-in cameras) of approximately $31 \text{nT} \mu\text{m}^{3/2}/\sqrt{\text{Hz}}$ [31,32]. Considering these limits, future improvements may involve lock-in-based detection to boost the sensitivity and pulse sequences for T1 relaxometry [18].

ACKNOWLEDGMENTS

This work was supported by the German Federal Ministry of Education and Research (BMBF) within the Quantumtechnologien program (DIAQNOS, Project No. 13N16455) and by the European Commission Horizon Europe Framework Program under the Research and Innovation Action MUQUABIS, Project No. 101070546.

- [1] J. R. Maze, A. Gali, E. Togan, Y. Chu, A. Trifonov, E. Kaxiras, and M. D. Lukin, Properties of nitrogen-vacancy centers in diamond: The group theoretic approach, *New J. Phys.* **13**, 025025 (2011).
- [2] M. Lesik, T. Plisson, L. Toraille, J. Renaud, F. Occelli, M. Schmidt, O. Salord, A. Delobbe, T. Debuisschert, L. Rondin, P. Loubeyre, and J.-F. Roch, Magnetic measurements on micrometer-sized samples under high pressure using designed NV centers, *Science* **366**, 1359 (2019).
- [3] V. M. Acosta, E. Bauch, M. P. Ledbetter, A. Waxman, L.-S. Bouchard, and D. Budker, Temperature dependence of the nitrogen-vacancy magnetic resonance in diamond, *Phys. Rev. Lett.* **104**, 070801 (2010).
- [4] A. Jarmola, V. M. Acosta, K. Jensen, S. Chemerisov, and D. Budker, Temperature- and magnetic-field-dependent longitudinal spin relaxation in nitrogen-vacancy ensembles in diamond, *Phys. Rev. Lett.* **108**, 197601 (2012).
- [5] G. Chatzidrosos, A. Wickenbrock, L. Bougas, N. Leefer, T. Wu, K. Jensen, Y. Dumeige, and D. Budker, Miniature cavity-enhanced diamond magnetometer, *Phys. Rev. Appl.* **8**, 044019 (2017).
- [6] J. F. Barry, M. J. Turner, J. M. Schloss, D. R. Glenn, Y. Song, M. D. Lukin, H. Park, and R. L. Walsworth, Optical magnetic detection of single-neuron action potentials using quantum defects in diamond, *Proc. Natl. Acad. Sci.* **113**, 14133 (2016).
- [7] J. F. Barry, M. H. Steinecker, S. T. Alsid, J. Majumder, L. M. Pham, M. F. O’Keefe, and D. A. Braje, Sensitive ac and dc magnetometry with nitrogen-vacancy center ensembles in diamond (2023).
- [8] M. Karadas, A. M. Wojciechowski, A. Huck, N. O. Dalby, U. L. Andersen, and A. Thielscher, Feasibility and resolution limits of opto-magnetic imaging of neural network

- activity in brain slices using color centers in diamond, *Sci. Rep.* **8**, 4503 (2018).
- [9] J. L. Webb, L. Troise, N. W. Hansen, C. Olsson, A. M. Wojciechowski, J. Achard, O. Brinza, R. Staacke, M. Kieschnick, J. Meijer, A. Thielscher, J.-F. Perrier, K. Berg-Sørensen, A. Huck, and U. L. Andersen, Detection of biological signals from a live mammalian muscle using an early stage diamond quantum sensor, *Sci. Rep.* **11**, 2412 (2021).
- [10] T. Lenz, G. Chatzidrosos, Z. Wang, L. Bougas, Y. Dumeige, A. Wickenbrock, N. Kerber, J. Zázvorka, F. Kammerbauer, M. Kläui, Z. Kazi, K.-M. C. Fu, K. M. Itoh, H. Watanabe, and D. Budker, Imaging topological spin structures using light-polarization and magnetic microscopy, *Phys. Rev. Appl.* **15**, 024040 (2021).
- [11] E. V. Levine, M. J. Turner, P. Kehayias, C. A. Hart, N. Langellier, R. Trubko, D. R. Glenn, R. R. Fu, and R. L. Walsworth, Principles and techniques of the quantum diamond microscope, *Nanophotonics* **8**, 1945 (2019).
- [12] M. W. Doherty, F. Dolde, H. Fedder, F. Jelezko, J. Wrachtrup, N. B. Manson, and L. C. L. Hollenberg, Theory of the ground-state spin of the NV⁻ center in diamond, *Phys. Rev. B* **85**, 205203 (2012).
- [13] V. Ivády, H. Zheng, A. Wickenbrock, L. Bougas, G. Chatzidrosos, K. Nakamura, H. Sumiya, T. Ohshima, J. Isoya, D. Budker, I. A. Abrikosov, and A. Gali, Photoluminescence at the ground-state level anticrossing of the nitrogen-vacancy center in diamond: A comprehensive study, *Phys. Rev. B* **103**, 035307 (2021).
- [14] A. Wickenbrock, H. Zheng, L. Bougas, N. Leefer, S. Afach, A. Jarmola, V. M. Acosta, and D. Budker, Microwave-free magnetometry with nitrogen-vacancy centers in diamond, *Appl. Phys. Lett.* **109**, 053505 (2016).
- [15] M. Auzinsh, A. Berzins, D. Budker, L. Busaite, R. Ferber, F. Gahbauer, R. Lazda, A. Wickenbrock, and H. Zheng, Hyperfine level structure in nitrogen-vacancy centers near the ground-state level anticrossing, *Phys. Rev. B* **100**, 075204 (2019).
- [16] H. Zheng, Z. Sun, G. Chatzidrosos, C. Zhang, K. Nakamura, H. Sumiya, T. Ohshima, J. Isoya, J. Wrachtrup, A. Wickenbrock, and D. Budker, Microwave-free vector magnetometry with nitrogen-vacancy centers along a single axis in diamond, *Phys. Rev. Appl.* **13**, 044023 (2020).
- [17] X. Zhang, G. Chatzidrosos, Y. Hu, H. Zheng, A. Wickenbrock, A. Jerschow, and D. Budker, Battery characterization via eddy-current imaging with nitrogen-vacancy centers in diamond, *Appl. Sci.* **11**, 3069 (2021).
- [18] J. D. A. Wood, J.-P. Tetienne, D. A. Broadway, L. T. Hall, D. A. Simpson, A. Stacey, and L. C. L. Hollenberg, Microwave-free nuclear magnetic resonance at molecular scales, *Nat. Commun.* **8**, 15950 (2017).
- [19] H. Zheng, G. Chatzidrosos, A. Wickenbrock, L. Bougas, R. Lazda, A. Berzins, F. H. Gahbauer, M. Auzinsh, R. Ferber, and D. Budker, Level anti-crossing magnetometry with color centers in diamond (2017).
- [20] A. Wickenbrock, H. Zheng, G. Chatzidrosos, J. S. Rebeirro, T. Schneemann, and P. Blümler, High homogeneity permanent magnet for diamond magnetometry, *J. Magn. Reson.* **322**, 106867 (2021).
- [21] G. Chatzidrosos, J. S. Rebeirro, H. Zheng, M. Omar, A. Brenneis, F. M. Stürner, T. Fuchs, T. Buck, R. Röller, T. Schneemann, P. Blümler, D. Budker, and A. Wickenbrock, Fiberized diamond-based vector magnetometers, *Front. Photonics* **2**, 732748 (2021).
- [22] S. C. Scholten, A. J. Healey, I. O. Robertson, G. J. Abrahams, D. A. Broadway, and J.-P. Tetienne, Widefield quantum microscopy with nitrogen-vacancy centers in diamond: Strengths, limitations, and prospects, *J. Appl. Phys.* **130**, 150902 (2021).
- [23] L. Petrakis, Spectral line shapes: Gaussian and Lorentzian functions in magnetic resonance, *J. Chem. Educ.* **44**, 432 (1967).
- [24] S. Anishchik and K. Ivanov, A method for simulating level anti-crossing spectra of diamond crystals containing NV⁻ color centers, *J. Magn. Reson.* **305**, 67 (2019).
- [25] S. Sengottuvvel, M. Mrózek, M. Sawczak, M. J. Głowacki, M. Ficek, W. Gawlik, and A. M. Wojciechowski, Wide-field magnetometry using nitrogen-vacancy color centers with randomly oriented micro-diamonds, *Sci. Rep.* **12**, 17997 (2022).
- [26] K. Levenberg, A method for the solution of certain nonlinear problems in least squares, *Q. Appl. Math.* **2**, 164 (1944).
- [27] S. W. Hell and J. Wichmann, Breaking the diffraction resolution limit by stimulated emission: Stimulated-emission-depletion fluorescence microscopy, *Opt. Lett.* **19**, 780 (1994).
- [28] E. Rittweger, K. Y. Han, S. E. Irvine, C. Eggeling, and S. W. Hell, STED microscopy reveals crystal colour centres with nanometric resolution, *Nat. Photonics* **3**, 144 (2009).
- [29] A. M. Wojciechowski, M. Karadas, A. Huck, C. Osterkamp, S. Jankuhn, J. Meijer, F. Jelezko, and U. L. Andersen, Contributed review: Camera-limits for wide-field magnetic resonance imaging with a nitrogen-vacancy spin sensor, *Rev. Sci. Instrum.* **89**, 031501 (2018).
- [30] C. Osterkamp, M. Mangold, J. Lang, P. Balasubramanian, T. Teraji, B. Naydenov, and F. Jelezko, Engineering preferentially-aligned nitrogen-vacancy centre ensembles in CVD grown diamond, *Sci. Rep.* **9**, 5786 (2019).
- [31] Z. Kazi, I. M. Shelby, H. Watanabe, K. M. Itoh, V. Shuttanandan, P. A. Wiggins, and K.-M. C. Fu, Wide-field dynamic magnetic microscopy using double-double quantum driving of a diamond defect ensemble, *Phys. Rev. Appl.* **15**, 054032 (2021).
- [32] C. A. Hart, J. M. Schloss, M. J. Turner, P. J. Scheidegger, E. Bauch, and R. L. Walsworth, NV-diamond magnetic microscopy using a double quantum 4-Ramsey protocol, *Phys. Rev. Appl.* **15**, 044020 (2021).